

# Electron number density measurements from the frequency shift of a plasma defect state in a one-dimensional photonic crystal

David Z. Pai<sup>1,a</sup>, Fabio Righetti<sup>2</sup>, Benjamin C. Wang<sup>2</sup>, David R. Biggs<sup>2</sup>, and Mark A. Cappelli<sup>2,b</sup>

<sup>1</sup> Institut Pprime (CNRS UPR 3346–Université de Poitiers–ENSMA), 86962 Chasseneuil Futuroscope, France

<sup>2</sup> Stanford Plasma Physics Laboratory, Department of Mechanical Engineering, Stanford University, Stanford, California 94305, USA

Received 14 December 2018 / Received in final form 1 February 2019

Published online 14 May 2019

© EDP Sciences / Società Italiana di Fisica / Springer-Verlag GmbH Germany, part of Springer Nature, 2019

**Abstract.** We describe the use of a plasma-functionalized vacancy defect in a one-dimensional microwave photonic crystal to experimentally measure the electron number density of glow discharges at 5–40 torr. The photonic crystal consists of spaced alumina plates with a built-in void defect that breaks the repeating symmetry of the layers, resulting in narrow defect transmission peaks within relatively deep bandgaps. We exploit the sensitivity of the defect transmission at 28 GHz to varying plasma density to measure electron number densities as low as  $2 \times 10^9 \text{ cm}^{-3}$ . Defect energy shifts are proportional to plasma density, in reasonable agreement with theoretical predictions of photonic crystal performance. At higher discharge current densities and discharge pressure, we see a departure from the model predictions, largely attributable to the heating of the alumina structure, causing expansion and changes in the lattice parameter that counteract the effect of the increased plasma density on the defect state frequency.

## 1 Introduction

Knowledge of the electron number density ( $n_e$ ) is essential to the characterization of low-temperature plasmas of relatively high collisionality with the electron collision frequency greater than the plasma frequency ( $\nu_c > \omega_p$ ). However, the measurement of this parameter can be difficult for a number of reasons, as reviewed recently in the literature [1] and briefly summarized here. First, standard diagnostics often used at low pressure (such as Langmuir and hairpin resonator probes) are intrusive and are not suited to the oftentimes small dimensions of high-pressure plasmas. At low pressure, under weak collisionality conditions, assumptions can be made to simplify the interpretation of measurements. At high pressure, there is currently no established theory that accounts for the effect of electron collisions in the plasma sheath. There are several diagnostic techniques whose interpretation is relatively straightforward, but which are costly and/or difficult to implement, as is the case for laser Thomson scattering [2], infrared heterodyne interferometry [3], and millimeter wave interferometry [4]. If the electric field can be determined accurately, such as by anti-Stokes Raman scattering, then  $n_e$  can be deduced [5]. The electron number density can also be deduced from the Stark broadening of atomic lines (if available) measured using optical

emission spectroscopy [6], which is comparatively straightforward to perform. However, this diagnostic is limited in range: if the electron number density is too low, then the Stark broadening contribution is difficult to detect. If  $n_e$  is too high then the correspondingly high ion density also contributes to Stark broadening, thus complicating the analysis of results. In this case, it is advisable to cross-check with an independent diagnostic, such as the electrical conductivity of the plasma, which itself requires making assumptions about the state of the plasma [7,8].

There is therefore a need for additional methods suitable to high-pressure plasmas that are straightforward in terms of both implementation and analysis, particularly for  $n_e < 10^{11} \text{ cm}^{-3}$ . The scattering or transmission of microwave or millimeter waves has recently been investigated for electron density measurements [9] and holds promise for such a diagnostic. The use of microwave scattering can be useful for atmospheric-pressure microplasmas, but calibration against objects with known dielectric constants is required [10]. Recently, measurements of the electron number density have emerged from studies on a single plasma inserted into a photonic crystal [11] and a microplasma array forming a photonic crystal [12]. In these studies, the diagnostic is based on the transmission of the probe signal rather than its scattering.

In this work, we investigate the use of one-dimensional plasma photonic crystals for the measurement of the electron density of moderate-pressure AC plasmas in argon. We build upon the work of [11], who demonstrated that

<sup>a</sup> e-mail: [david.pai@univ-poitiers.fr](mailto:david.pai@univ-poitiers.fr)

<sup>b</sup> e-mail: [cap@stanford.edu](mailto:cap@stanford.edu)

photonic crystals can be used to measure low electron densities. In their case, a columnar volume plasma was inserted as a defect inside a 2D photonic crystal formed by an array of dielectric rods. In this paper, we describe the case where we instead insert a planar AC discharge into a 1D photonic crystal consisting of a series of dielectric slabs. Also, by reducing the dimensionality to 1D, it is simpler to analyze experimental results, since the dispersion relation for 1D photonic crystals can be readily obtained [13], and the effects stemming from a lossy photonic crystal have already been investigated for this case [12]. A lossy crystal would result from the presence of a collisional plasma, which would be the case of an atmospheric-pressure plasma. Both dimensionality and collisionality were suggested as possible explanations for the discrepancy between experiments and modeling in [11], and therefore a 1D study would be beneficial to gaining insight into these issues. Previous studies on 1D plasma photonic crystals have included plasmas in every crystal unit rather than only in a defect, using discharges that were columnar rather than planar in shape [14,15].

## 2 Experimental setup and methods

The complete experimental setup is shown in Figure 1 (top), and its various components will be discussed in the following sections. We also present the electrical characterization of the plasma source in Section 2.2. We consider this source to be a generic plasma under study for evaluating our diagnostic technique. This plasma is not original, and we therefore do not characterize its properties further in Section 4, aside from the electron number density.

### 2.1 Photonic crystal

The high-index layers of the crystal consist of  $50\text{ mm} \times 50\text{ mm}$  square alumina (99.6% purity) plates of  $750\ \mu\text{m}$  thickness. The thickness of the alumina layers is adjusted by stacking these plates. The low-index layers consist of argon (99.995%) at various pressures. The thickness of the argon layers is adjusted by stacking metal-free PCB spacers of 1.4 mm thickness each. Figure 1 (bottom) shows the structure of the crystal that will later include the plasma defect. Each unit cell of the crystal is a bilayer formed by two alumina plates (1.4 mm total thickness) and two PCB spacers (2.8 mm total thickness). The crystal is 8 bilayers long, but a void defect has been built into it that is one PCB spacer (1.4 mm) thick and whose state (i.e. dielectric constant) can be altered by the presence of the plasma.

The crystal is held together by compression in an acrylic jig with nylon bolts. There are no metal parts in the core of the crystal that would produce unwanted scattering of microwave or terahertz radiation. Also, the jig has a large aperture, and the PCB spacers are small and placed at the corners of the alumina squares (Fig. 2a), thus ensuring the largest possible clear aperture for the passage of electromagnetic beams.

We examine crystals with different unit cell compositions, as well as the effect of inserting a void defect, with

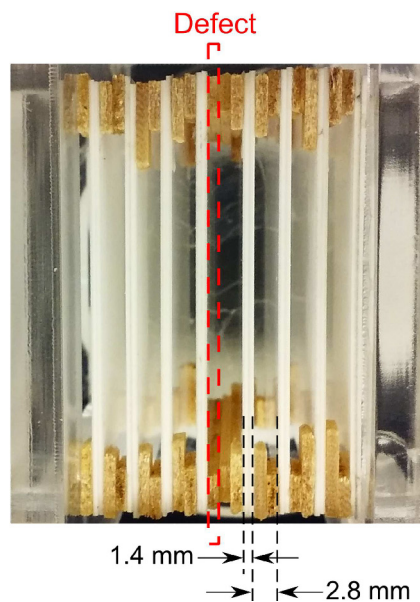
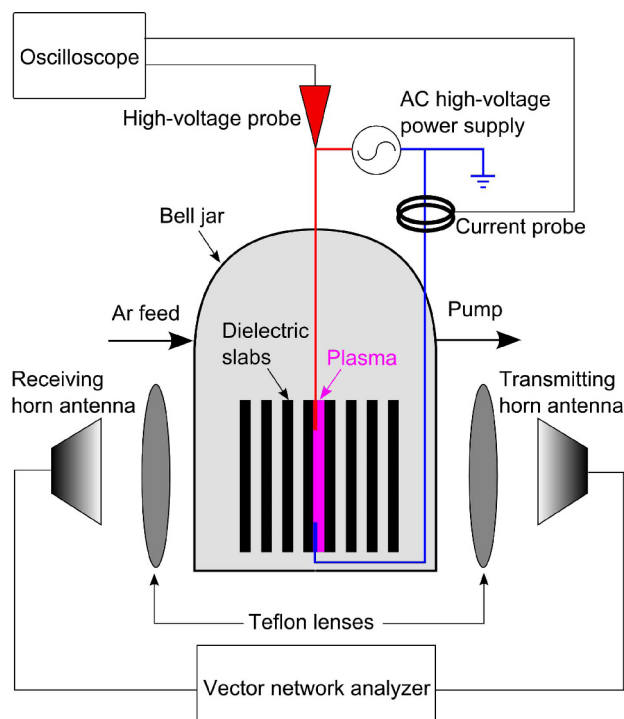


**Fig. 1.** Schematic diagram of the experimental setup (top). A series of dielectric slabs forms the 1D photonic crystal, with a plasma defect. The horn antennas are used to probe the microwave transmission characteristics of the crystal. Also shown is a side view image of the crystal (bottom), with 4 unit cells on either side of a void defect, which manifests itself by the increased thickness of the gas gap at the center of the crystal. The plasma reactor is placed on one of the interior alumina faces of this enlarged gas gap.

and without the presence of plasma. It will be shown in the following that microwave transmission through the crystal is sufficiently sensitive to the state of this plasma defect for measuring its electron number density.

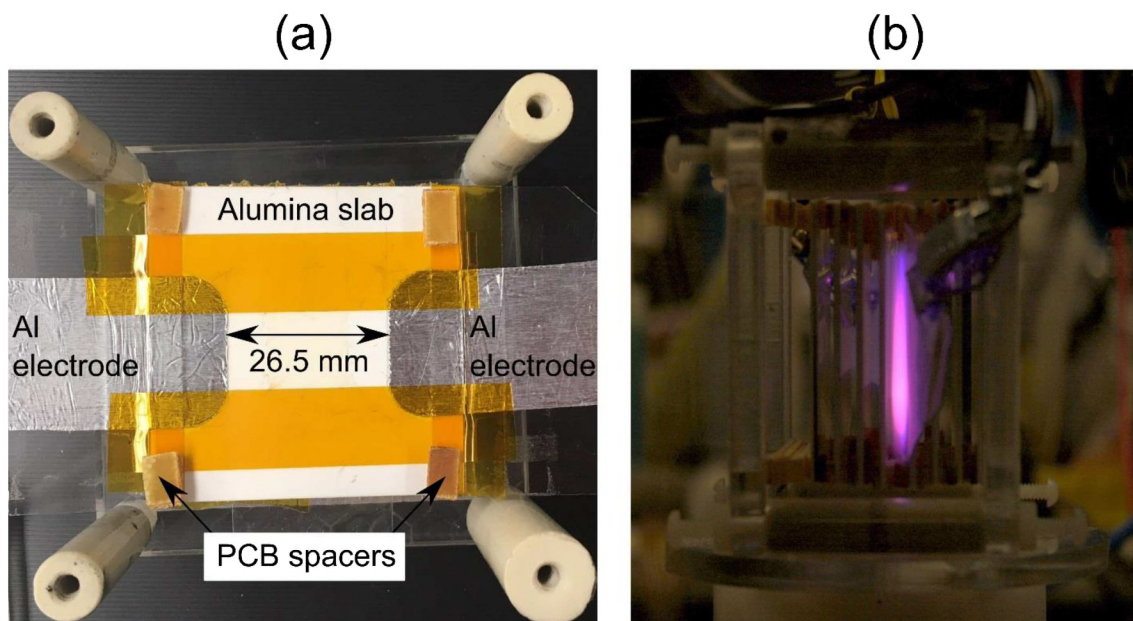


**Fig. 2.** (a) Top view of the plasma reactor, showing the 26.5 mm discharge gap. (b) Images of the 1D photonic crystal (8-unit) with a plasma defect inserted in the middle of the crystal, for typical conditions ( $p = 5$  torr, RMS current 5–45 mA). The image has been adjusted in contrast and brightness to show the location of the plasma, relative to the crystal structure.

## 2.2 Discharge circuit

The plasma defect is generated by taping two aluminum electrodes on the same side of one of the alumina plates facing the defect, as shown in Figure 2a. A rectangular discharge gap is formed with an inter-electrode distance of 26.5 mm. The electrode span is about 12 mm, but the plasma extends well beyond this length in the lateral dimension, as can be seen in Figure 2b, to about 40 mm. The high-voltage electrode is connected to an AC high-voltage generator (Model PVM400, Information Unlimited), and the other electrode is grounded. The crystal and its jig are placed inside a bell jar that is equipped with low-pressure feedthroughs for electrical connections. The bell jar is pumped down to vacuum before argon is introduced at the desired pressure.

The discharge produced is thus an AC glow plasma in moderate-pressure argon, without any dielectric barrier, that tends to fill the space between alumina slabs, as shown in Figure 2b. Under the typical operating conditions of  $p = 5$  torr and current amplitudes greater than a few mA, the plasma fills the void defect, as well as the gas portion of the adjacent crystal unit (Fig. 1, bottom). If the current is only a few mA, then the filling is incomplete. At high pressure, e.g. 40 torr, the plasma becomes localized.

The voltage and current are measured outside the bell jar using passive voltage (Tektronix model P6015) and Rogowski coil current (Pearson Electronics model 2877) probes, respectively. In “typical” operating conditions, the voltage assumes an irregular AC waveform with a frequency of 20 kHz (Fig. 3). As the voltage generator does not compensate for its load, the coupling to the plasma affects the output voltage. Nevertheless, the overall profile

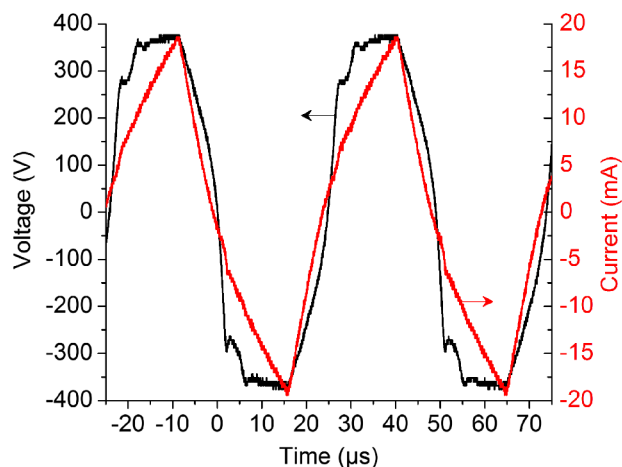


**Fig. 3.** Examples of measured voltage and current waveforms in “typical” operating conditions of  $p = 5$  torr and current amplitudes greater than a few mA.

is preserved, and in any case the specific voltage waveform is of minimal consequence in this study. Likewise, the current waveform generally assumes a nearly triangular profile whose specific form is not important. Since the voltage and current waveforms are largely in-phase, we can assume that the circuit is resistive, and so the capacitive current can be neglected in this case.

The “low-current” case merits special attention because it will be used to demonstrate the lower limit of the electron number density measurement technique that we will discuss in Section 4.3. As shown in Figure 4 (top), the voltage waveform becomes closer to a sinusoid with a frequency of about 63 kHz. By applying a 200 kHz low-pass FFT filter, the noise can be removed without affecting the

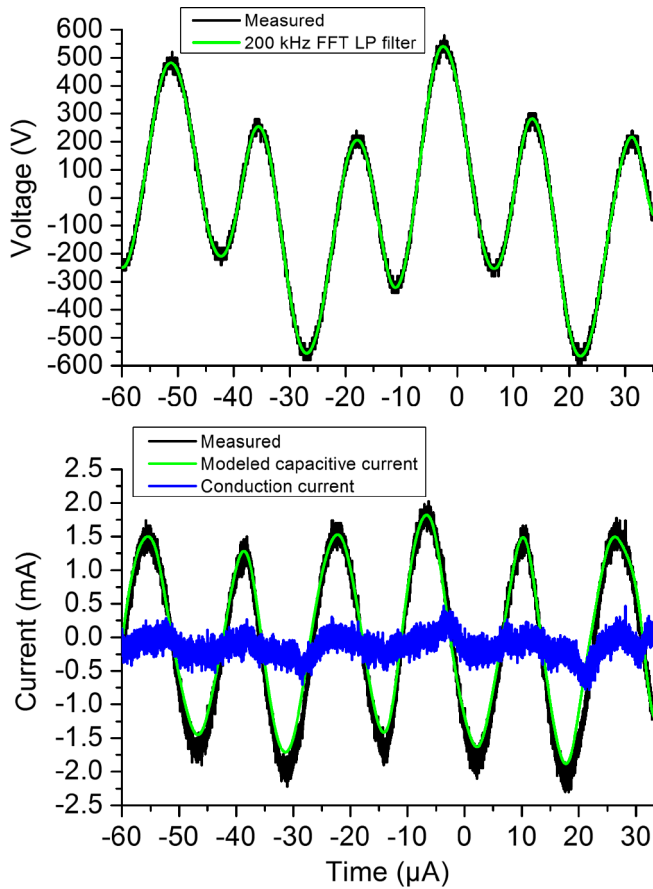


**Fig. 4.** Measured and filtered voltage waveforms for the “low-current” case at  $p = 5$  torr (top). The filtered voltage waveform is used to calculate the capacitive current, which is then subtracted from the measured current to obtain the conduction current (bottom).

integrity of the waveform. This filtered waveform can then be used to calculate the capacitive current, which can be subtracted off the measured current to obtain the conduction current (Fig. 4, bottom). The conduction current amplitude does not exceed 1 mA in this case, which is far smaller than the “typical” case and is consistent with the limited size of this discharge, as mentioned previously.

The applied voltage waveform and frequency change between the typical and low-current cases depending on the setting chosen for the power supply, which as mentioned above does not perform any matching with the plasma load. The resonant (output) frequency of the power supply is then load-dependent and uncontrolled, although this is unimportant for the purposes of this work. As a result, at a certain setting the plasma coupling with the power supply is such that its frequency is 63 kHz, and the current is low. At other settings, the coupling results in a frequency of 22 kHz, and the current is higher.

### 2.3 Microwave and terahertz transmission

Two different setups are used to characterize the plasma photonic crystal. First, a terahertz transmitter/receiver

device (Terascan, Toptica Photonics AG) is used to measure transmission from 30 to 600 GHz. Here we will only summarize its use for this work. The transmitting and receiving mirrors are placed at a distance of 50 cm from each other, enabling 0.7 GHz resolution. This low resolution, along with its relatively low dynamic range, prevents us from using this device to measure electron number density. However, the main purpose for using this device will be to validate the model of the crystal (Sect. 4.1) over a wide frequency range, which will be critical to relating the shift of the transmission peak of the defect state to the electron number density of the plasma (Sect. 4.2).

The second setup is a microwave transmitter/receiver device previously used in [11]. In our case, the beam is adjusted for proper passage through the crystal using Teflon lenses of 151.5 mm focal length (Thorlabs LAT151). With this focal length, and assuming a plane wave propagating onto the 10 cm diameter lens, we find a depth of focus of about 15 cm that greatly exceeds the length of the crystal. Thus, field divergence within the crystal should not have a significant effect on the results. This system will be used to probe the plasma defect, whose transmission peak falls within the sweep range of the device. Also, its spectral resolution and dynamic range are sufficiently high for resolving the defect peak.

## 3 Model

We employ a simple 1D transfer matrix method to model the photonic crystal. It is a straightforward application of the formalism presented in [16] (Chap. 5), coded in Python (x, y). Transmission and reflection coefficients are calculated at each alumina/gas interface, starting from the crystal exit and progressively computed in the direction opposite of wave propagation. The plasma defect is modeled only as a slab with complex permittivity, following [11,17]. The mathematical description of the model can be found in the appendix.

When accounting for the plasma, the index of refraction of the defect slab is calculated using the plasma permittivity ( $\epsilon_p$ ) based on the Drude model:

$$\epsilon_p = 1 - \frac{\omega_p^2}{\omega^2 - j\nu_{eh}\omega} \quad (1)$$

where the plasma frequency ( $\omega_p$ ) and electron-neutral collision frequency ( $\nu_{eh}$ ) are:

$$\omega_p = \sqrt{\frac{n_e e^2}{m_e \epsilon_0}} \quad (2)$$

$$\nu_{eh} = N \sigma_{eh} \nu_e \quad (3)$$

Here  $m_e$  is the mass of the electron,  $\epsilon_0$  is the permittivity of free space, and  $N$  is the neutral gas density. The cross-section for electron-neutral collisions is taken to be  $\sigma_{eh} = 10^{-19} \text{ m}^2$ . The mean electron velocity  $\nu_e$  is:

$$\nu_e = \sqrt{\frac{8k_B T_e}{\pi m_e}} \quad (4)$$

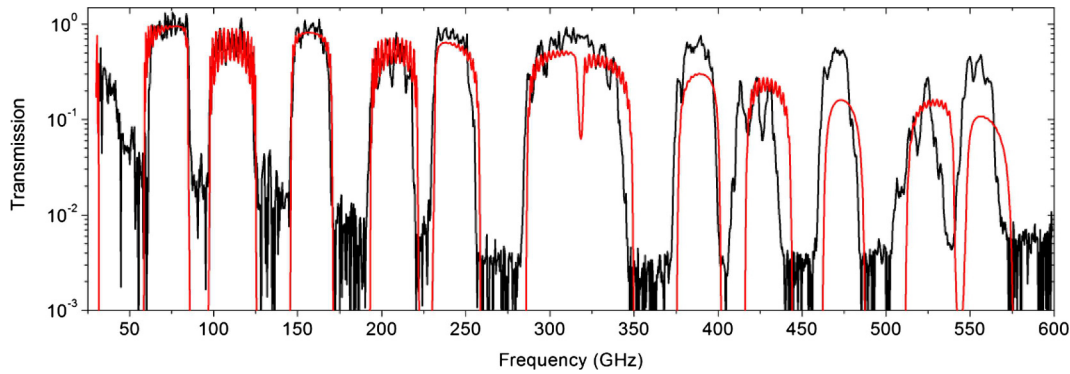


**Fig. 5.** Experimental and modeled transmission spectra for a 16-unit pure crystal with no defect. Unit cell: alumina thickness = 0.7 mm, gas thickness = 1.4 mm.

where  $k_B$  is Boltzmann's constant, and  $T_e$  is the electron temperature.

In the next section, the model will be used to calculate the transmission spectrum for different crystal structures. The insertion of defects into the crystal results in the appearance of sharp transmission peaks in the bandgaps. The peak position shifts with the defect size and electron number density. The calculation of the shift via the model, along with measurements, will be the key to extending measurable shifts down to low electron number densities.

## 4 Results and discussion

### 4.1 Experimental validation of the model

We test the model against several experimental crystal structures, without plasma. First, we constructed a pure crystal with 16 unit cells (16-unit) and measured its transmission spectrum up to 600 GHz, as shown in Figure 5. The band structure is well modeled in both band position and relative amplitude up to about 250 GHz, covering the first five pass bands. Above 250 GHz, the model loses quantitative agreement with experiment, but the overall band structure is reproduced. The modeled bandgaps are deeper than in experiment due to the noise floor of the terahertz spectrometer. In order to achieve such agreement, the index of refraction of the alumina was chosen to be 2.72 in the model, which is lower than the nominal value of 3 typical of 99.6% alumina. The loss tangent of alumina is also modeled, accounting for the gradual decrease in transmission with frequency. It should be noted that the dielectric constant of alumina does not vary significantly over this frequency range [18].

One reason for the discrepancy in index of refraction may be that the beam diameter is comparable to the size of the crystal face, particularly at lower frequencies. Thus, the beam may overlap both the alumina and the gas surrounding the crystal. As a result, the effective index of refraction may be lowered by the gas around the alumina. The poor agreement of the model at high frequencies may be because the beam profile changes with frequency. As a result, the beam may not be equally collimated and/or aligned at all frequencies. Such deviations from the ideal

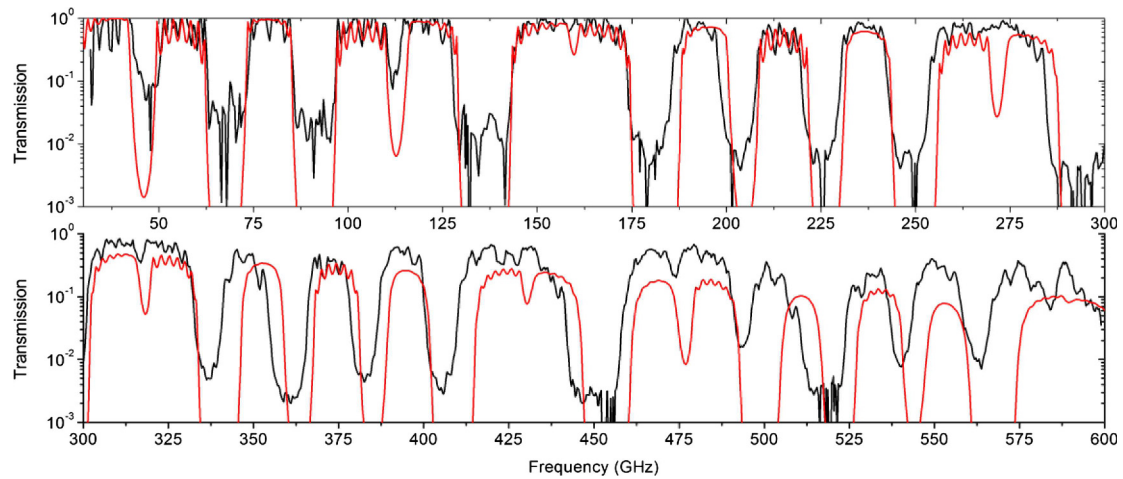
beam profile would result in some energy being lost in the transverse direction, which we do not account for in the 1D model.

Figure 6 shows the experimental and modeled transmission spectra of a pure 8-unit crystal, where the unit cell dimensions have been scaled up by a factor of 2 compared to the previous 16-unit crystal. Aside from the unit cell dimensions, there are no changes to the model used in Figure 5. Again, there is reasonable quantitative agreement on band position and relative amplitude up to about 250 GHz. Since the crystal is larger in dimension, this range covers the first nine pass bands. Like before, only the band structure is well modeled above 250 GHz.

Figure 7 shows the results for the same 8-unit crystal as in Figure 6, except with a defect inserted in the middle, i.e. with a 4-unit crystal on both sides of the defect. The defect is a "void" with an index of refraction of 1 and a thickness of 1.4 mm. This is the structure shown in Figure 1. Except for the addition of the defect, the model is the same as that used in Figure 6. The same observations concerning the agreement of the model with experiment in Figures 5 and 6 apply here. In addition, the model predicts defect peaks at 45, 86, 179, 251, 363, and 386 GHz that also appear in experiment (Figs. 6 and 7).

Finally, for measuring frequency shift as a function of electron number density, in Figure 8 we zoom in on the defect peak of interest, which is found at 28 GHz using the 8-unit crystal from Figure 7. Unlike for Figure 5 through Figure 7, the microwave system is used rather than the terahertz system. Because of the better resolution and sensitivity of the former, the defect peak is readily detectable with an amplitude about 10 dBm above the bottom of the first bandgap. The model is unchanged from that used for Figure 7. The defect peak position is within 1 GHz of its experimental value, and the band edge is well modeled. The model also presents a dip at 33 GHz inside the pass band, but the experimental dip is deeper and wider.

The model thus performs satisfactorily, particularly at low frequencies less than 250 GHz. Only the index of refraction of alumina needed to be fitted to the data. Otherwise, measured dimensions have been used. By only changing the geometry of the crystal, four different experimental spectra have been modeled with a common set of parameters to a



**Fig. 6.** Experimental (black) and modeled (red) transmission spectra for a 8-unit pure crystal with no defect, in the 30–300 GHz range (top) and 300–600 GHz range (bottom). Unit cell: alumina thickness = 1.4 mm, gas thickness = 2.8 mm.

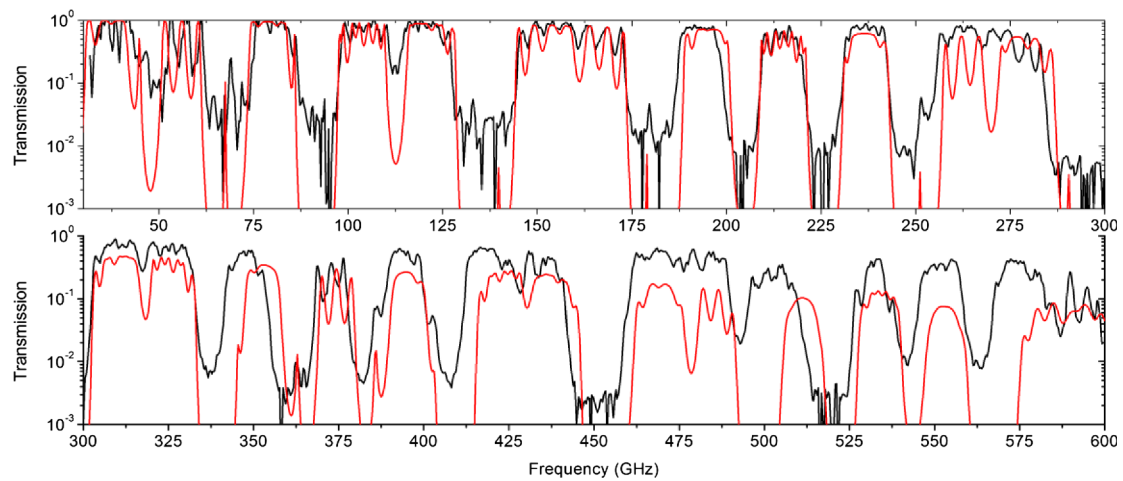


**Fig. 7.** Experimental (black) and modeled (red) transmission spectra for a 8-unit crystal, with an additional void defect inserted in the middle, in the 30–300 GHz range (top) and 300–600 GHz range (bottom). Unit cell: alumina thickness = 1.4 mm, gas thickness = 2.8 mm. Void defect: gas thickness = 1.4 mm.

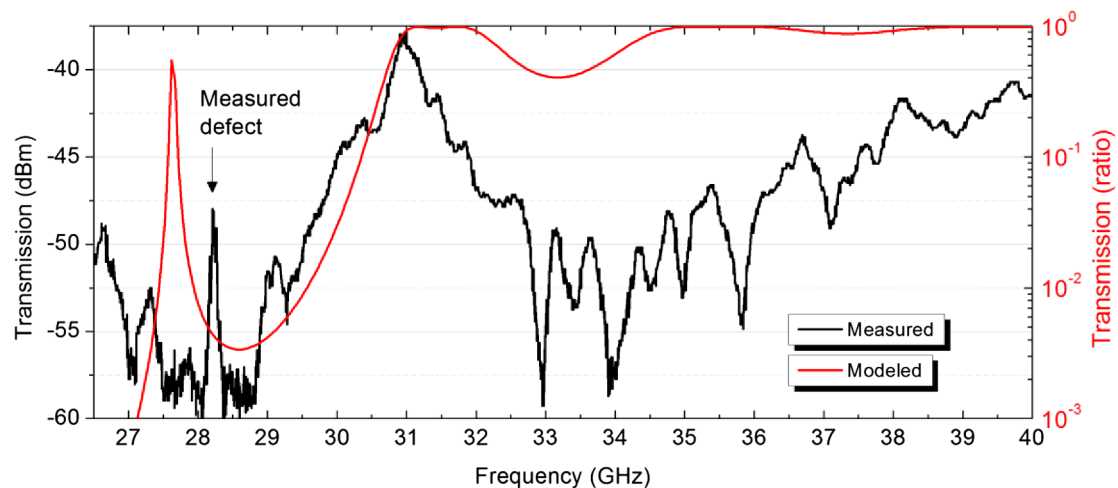


**Fig. 8.** Experimental and modeled transmission spectra for a 8-unit crystal, with an additional void defect inserted in the middle. The defect sits in the first bandgap. Unit cell: alumina thickness = 1.4 mm, gas thickness = 2.8 mm. Void defect: gas thickness = 1.4 mm.

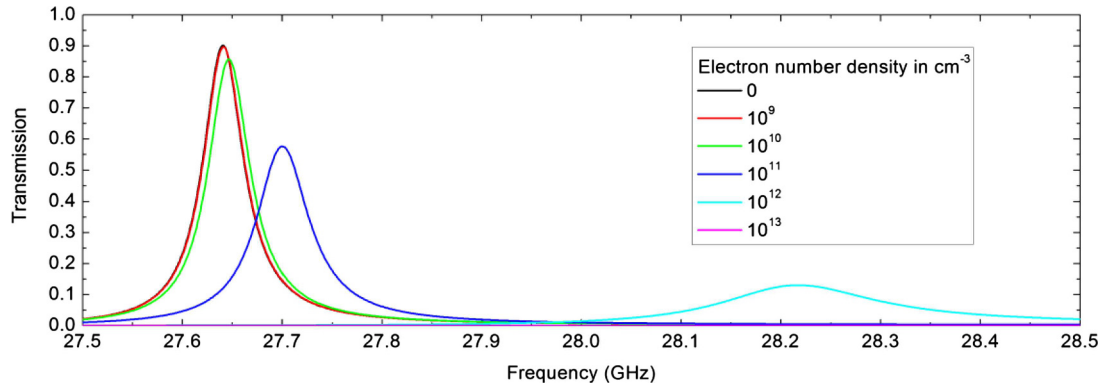


**Fig. 9.** Modeled transmission spectra of the first defect peak for the same 8-unit crystal as in Figure 7, except that the void is filled with plasma (Ar at 5 torr,  $T_e = 30\,000$  K) with different electron number densities.

reasonable degree of agreement. This model will be used in the next section to evaluate the shift of the defect peak as a function of the electron number density.

#### 4.2 Modeled frequency shift of the defect peak at 28 GHz

The generation of a plasma in the defect causes its transmission peak to shift in frequency, which we can model using the transfer matrix method presented previously. As mentioned in Section 2.2, the plasma not only fills the void defect but also the gas portion of the adjacent crystal cell. We account for this plasma volume in the model. For the 8-unit crystal with a void defect, the first defect peak at about 28 GHz is sharp ( $\sim 100$  MHz wide) and changes in both position and width with electron number density, as shown in Figure 9 for the case of a plasma modeled in argon at 5 torr and with an electron temperature of  $T_e = 30\,000$  K. The electron temperature determines the electron-neutral collision frequency, and this choice of  $T_e$  is typical for low-temperature plasmas, but in any case the results are not very sensitive to this parameter for our conditions, as we will see shortly.

Increasing the electron number density shifts the peak to higher frequency but also degrades its quality factor, such that by  $n_e = 10^{13}$  cm $^{-3}$  the defect peak is nonexistent. The peak position is most sensitive to  $n_e$  values between  $10^{10}$  and  $10^{12}$  cm $^{-3}$ , where both the peak integrity and degree of shift (spanning about 600 MHz) are high.

Provided that a small shift can be determined accurately by experiment, there is no theoretical impediment to determining the electron number density because the model has been validated. Figure 10 shows that the relationship between the shift relative to the no-plasma peak position is log-log linear over a wide range of  $n_e = 10^8$ – $10^{12}$  cm $^{-3}$ . As we will see in the next section, our microwave setup is able to resolve shifts down to about 1 MHz, which puts the detection limit at about  $n_e = 10^9$  cm $^{-3}$  with our current equipment.

Also shown in Figure 10 is the change in the frequency shift when the electron temperature increases from 30 000 to 100 000 K. The shift decreases by only about 2% over

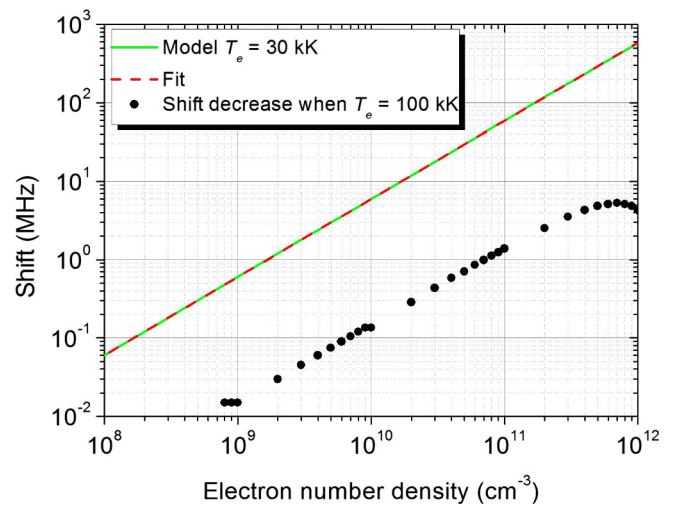


**Fig. 10.** Modeled shift of the defect peak frequency relative to the no-plasma frequency (solid line) for the same 8-unit crystal as in Figure 9, as well as a linear fit in log-log scale (dashed line), as a function of the electron number density for a plasma in Ar at 5 torr. Also shown is the change in shift when  $T_e$  increases from 30 to 100 kK. The shift is determined by the frequency of maximum transmission of the peak profile (Python library Peakutils, “indexes” algorithm).

much of the  $n_e$  range considered, becoming proportionally even smaller as  $n_e$  approaches  $10^{12}$  cm $^{-3}$ .

Figure 11 shows modeled shifts over the range relevant to this work, which correspond to electron number densities in the  $10^9$ – $10^{11}$  cm $^{-3}$  range, for pressures ranging from 5 torr to atmospheric pressure. In this limited range of  $n_e$ , a linear fit is appropriate at all pressures. The fitting coefficients shown in Table 1 can be used to readily calculate the shift for a given  $n_e$ . The slope of the lines, i.e. the sensitivity, decreases with increasing pressure. As expected, the effect of increased gas pressure is to increase the collisionality of the plasma and hence losses. The  $n_e$  range shown in Figure 11 is still rather low, and there are a number of atmospheric-pressure plasma sources with higher electron number densities that could potentially yield larger shifts.

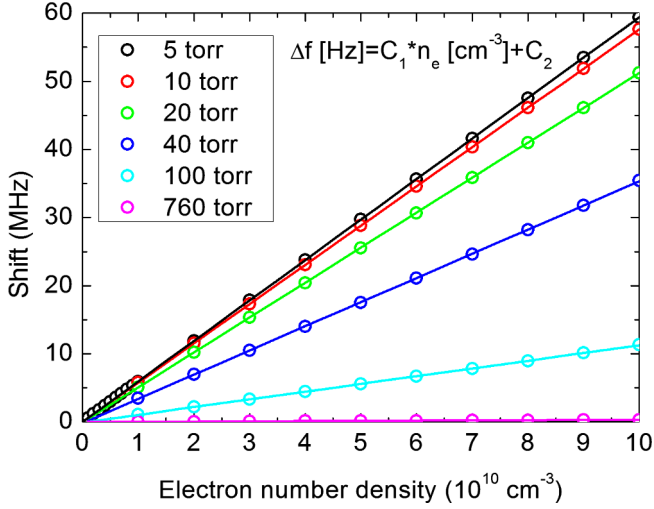


**Fig. 11.** Modeled shift of the defect peak frequency, relative to the no-plasma position, as a function of the electron number density for a plasma in Ar at different pressures. The shift was determined by the frequency of maximum transmission of the peak profile (Python library Peakutils, “indexes” algorithm). Also shown are linear fits of the modeled points. The fitting coefficients are  $C_1$  and  $C_2$  shown in Table 1.

### 4.3 Measured frequency shift of the defect peak at 28 GHz

We are now prepared to present and discuss measurements of the shift of the defect peak. Figure 12 shows the measured shift as a function of the RMS current ( $i_{\text{RMS}}$ ), and we see that shifts as small as about 1 MHz are measurable. At  $i_{\text{RMS}} = 50$  mA, the uncertainty becomes significant. The plasma may be heating the spacers and causing the defect to expand. A larger defect would have a lower no-plasma peak frequency. This downward shift would counter the upward shift induced by the plasma. Indeed, the thermal expansion coefficient of FR-4 glass epoxy is  $7 \times 10^{-5} \text{ K}^{-1}$  in the through-plane direction of a PCB board. If the PCB spacer heats up by 10 K, then it will expand by 0.07%. For  $n_e = 3 \times 10^{10} \text{ cm}^{-3}$ , the model predicts that this amount of expansion would shift the defect peak from 27.6944715 GHz to 27.6883471 GHz, a downward shift of 6.1 MHz. This corresponds well to the increased amount of uncertainty in the shift shown in Figure 12 at  $i_{\text{RMS}} = 50$  mA. Figure 12 also shows the corresponding electron number densities calculated via the linear fit shown in Figure 11. We see that it is possible to measure down to about  $n_e = 2 \times 10^9 \text{ cm}^{-3}$ .

We can compare the measured shifts to estimated values based on RMS values of the current and voltage, following [11]. Both measured and calculated values of the shift reflect space- and time-averaged values of  $n_e$ . RMS current-voltage measurements yield a calculation of  $n_e$ , which is then translated into a shift via the appropriate linear fit (Tab. 1). The calculation of  $n_e$  is based on  $j = en_e v_d$ , where  $j$  is the measured current density,  $e$  is the elementary charge, and  $v_d = \mu_e E$  is the electron drift velocity (where  $\mu_e$  is the electron mobility and  $E$

**Table 1.** Fitting coefficients of the linear fits shown in Figure 11 for different pressures.

Pressure	$C_1$	$C_2$
5	$5.94 \times 10^{-4}$	11543
10	$5.76 \times 10^{-4}$	15002
20	$5.13 \times 10^{-4}$	-61006
40	$3.55 \times 10^{-4}$	-155016
100	$1.13 \times 10^{-4}$	-84008
760	$3.15 \times 10^{-6}$	4000

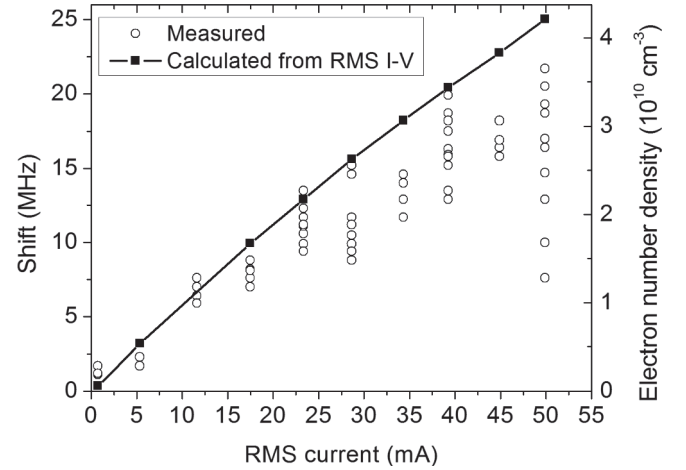


**Fig. 12.** Measured peak shifts of the photonic crystal defect shown in Figure 8, as a function of the RMS current of the plasma in Ar at 5 torr. Also shown is the calculated shift based on the RMS current/voltage values. The vertical axis on the right-hand side indicates the electron number density that corresponds to the shift, calculated using the linear fits shown in Figure 11.

is the electric field). The electron mobility in argon was calculated using BOLSIG+ via [www.lxcat.net](http://www.lxcat.net), using the SIGLO database [19,20]. To calculate the electric field, a cathode fall voltage drop of 100 V for Ar plasmas with Al electrodes [21] is subtracted off the RMS voltage value. To calculate the reduced electric field  $E/N$ , the nominal gas pressure is used, without taking into account the effect of localized plasma heating. The plasma is assumed to be uniform throughout a rectangular prism volume that covers a lateral span of 40 mm (as shown in Fig. 2b), traverses the discharge gap of 26.5 mm, and fills the 4.2 mm thick gas gap that includes the defect (Fig. 1). In reality, the spatial distribution of  $n_e$  is likely to occupy an ellipsoidal volume, bulging outward from the edges of the electrodes in the lateral direction and diminishing near the alumina walls in the longitudinal direction.

The calculated shifts agree well with the measurements at low RMS current but overshoot the experimental values at the highest current values. This discrepancy is probably not due to a thermal expansion of the defect via plasma heating, because the increased uncertainty in the shift measurements only occurs at  $i_{\text{RMS}} = 50$  mA and not at lower values. However, plasma heating may also cause the gas density to decrease, resulting in increased  $E/N$ . If

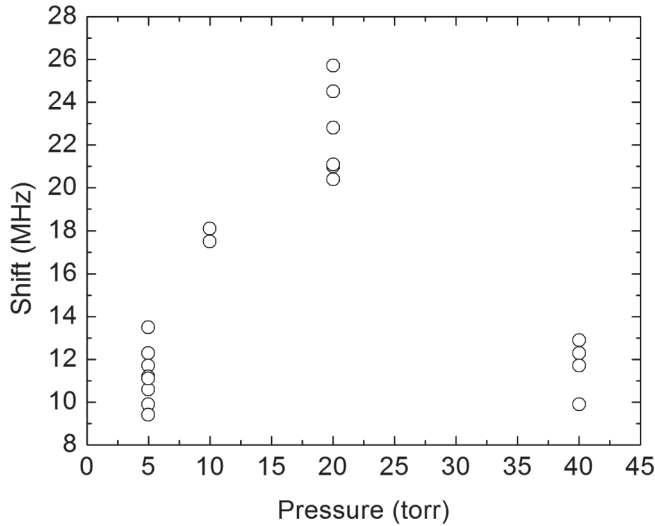


**Fig. 13.** Measured defect peak shifts as a function of pressure of the plasma in Ar, with the RMS current fixed at 23 mA.

known, using such values for  $E/N$  rather than the nominal values to calculate  $n_e$  from current-voltage measurements would lower the values of the calculated shifts, resulting in better agreement with the measured values. Finally, as mentioned in Section 2.2, the discharge does not fill or span the defect for the lowest-current case shown in Figure 12. Overestimating the cross-sectional area of the discharge would indeed depress the calculated shift below its true value.

Finally, in Figure 13 we examine the effect of pressure at a fixed RMS current of 23 mA. The shift increases from about 11 to 23 MHz with pressure from 5 to 20 torr, corresponding to an increase in  $n_e$  from about 2 up to  $4.5 \times 10^9 \text{ cm}^{-3}$ , according to Figure 11. From 5 to 20 torr, the RMS applied voltage is maintained in the range 275–299 V, thus the electron drift velocity should decrease from about 4 to  $1 \times 10^6 \text{ cm/s}$ . The electron number density should correspondingly increase by a factor of 4 but is measured to be less. Then, at 40 torr, the shift decreases back down to about 12 MHz, corresponding to  $n_e = 3.5 \times 10^9 \text{ cm}^{-3}$ . These discrepancies are likely due to assuming the nominal gas pressure (density) rather than the density upon gas heating by the plasma. However, as noted in Section 2.2, at 40 torr the plasma also tends to localize, causing the current density to be higher than otherwise. This may result in increased gas heating and a concomitant thermal expansion of the defect, suppressing the shift. Finally, the microwave beam waist is on the order of 5 cm, which is larger than the estimated transverse size of the plasma at high pressure. This means that a significant fraction of the waves will bypass the plasma, resulting in an underestimate of the plasma density.

#### 4.4 Effect of non-uniform electron number density

The results presented so far have presumed a uniform electron number density in the plasma defect. Here, we examine the effect of non-uniform  $n_e$  on microwave trans-

mission. A related problem was addressed by [22] for an all-plasma 1D crystal, but in that case  $n_e$  was assumed to be uniform in each plasma slab. We will introduce non-uniform  $n_e$  within a single plasma slab. To begin, we consider the electric field and energy density on and off the resonant frequency of the defect state for the case of uniform  $n_e$ . The electric field shown in Figure 14 (top) is in fact the real component of the phasor  $E$  in the 8-unit crystal:

$$E = E_+ + E_- = E_{+0} \exp(-jkz) + E_{-0} \exp(jkz) \quad (5)$$

where  $E_{+0}$  and  $E_{-0}$  are the amplitudes of forward- and backward-propagating waves, respectively, with wave vector  $k$ . Within a slab of the crystal, the amplitude of  $E$  remains constant but not  $\text{Re}\{E\}$ , the field value at phase  $kz$ . The electric field is concentrated in the regions of high index of refraction (i.e. alumina), with zero-field crossings within the gas gaps. As illustrated in [23] (Chap. 4, Fig. 4a) for a defect-free one-dimensional crystal with high dielectric contrast, such a profile corresponds to the mode at the top of the lower pass band adjacent to the bandgap. Thus, one of the modes from the lower pass band is pushed up into the bandgap by the defect. At the peak frequency of 27.7 GHz for  $n_e = 1 \times 10^{11} \text{ cm}^{-3}$  (see Fig. 9),  $\text{Re}\{E\}$  is more concentrated in the vicinity of the defect than at 27.5 or 27.9 GHz, which is consistent with a localized mode.

Figure 14 (bottom) shows the energy density  $\varepsilon|E|^2/2$ , whose value is constant within a slab. Like the electric field, the energy density is concentrated near the defect at the peak frequency of 27.7 GHz. As expected, most of the incoming energy  $\varepsilon|E_+(z = 35 \text{ mm})|^2/2$  is transmitted out of the crystal at  $z = 3 \text{ mm}$ , and little is reflected at  $z = 35 \text{ mm}$ . At 27.5 and 27.9 GHz, the opposite is true. Note that we are not showing the “local energy density” shown in [23] (Chap. 4, Fig. 4c), whose profile we can find for our case if we instead calculate  $\varepsilon \text{Re}\{E\}^2/2$ .

For the case of non-uniform  $n_e$  in the defect, we assume a parabolic profile with the maximum value  $n_{e,\text{max}}$  at  $z = z_{\text{max}}$ , the center of the defect gap with width  $D$ :

$$n_e = n_{e,\text{max}} \left[ 1 - (2(z - z_{\text{max}})/D)^2 \right]. \quad (6)$$

Figure 15 shows the resulting profile of the real component of the index of refraction for the same crystal as in Figure 14, except with a parabolic  $n_e$  profile according to equation (6) where  $n_{e,\text{max}} = 1.53125 \times 10^{11} \text{ cm}^{-3}$  and  $T_e = 30\,000 \text{ K}$ . This profile has an average density of  $n_e = 1 \times 10^{11} \text{ cm}^{-3}$ . With variable  $n_e$ , the field inside the defect becomes at most 24% higher relative to that of the incident wave, and the relative energy density decreases by up to 21%. The transmitted energy density also decreases by 20%. Unlike the uniform  $n_e$  case, the energy density does not remain constant inside the defect, decreasing by 2.4% from the edge to the middle. The effect of variable electron number density is thus moderate in terms of the electric field and energy density.

Figure 16 shows the effect of a parabolic  $n_e$  profile on the shift of the defect peak frequency. For the same average  $n_e$  value, the shift associated with a parabolic profile is only about 1% greater than that of a uniform profile. The

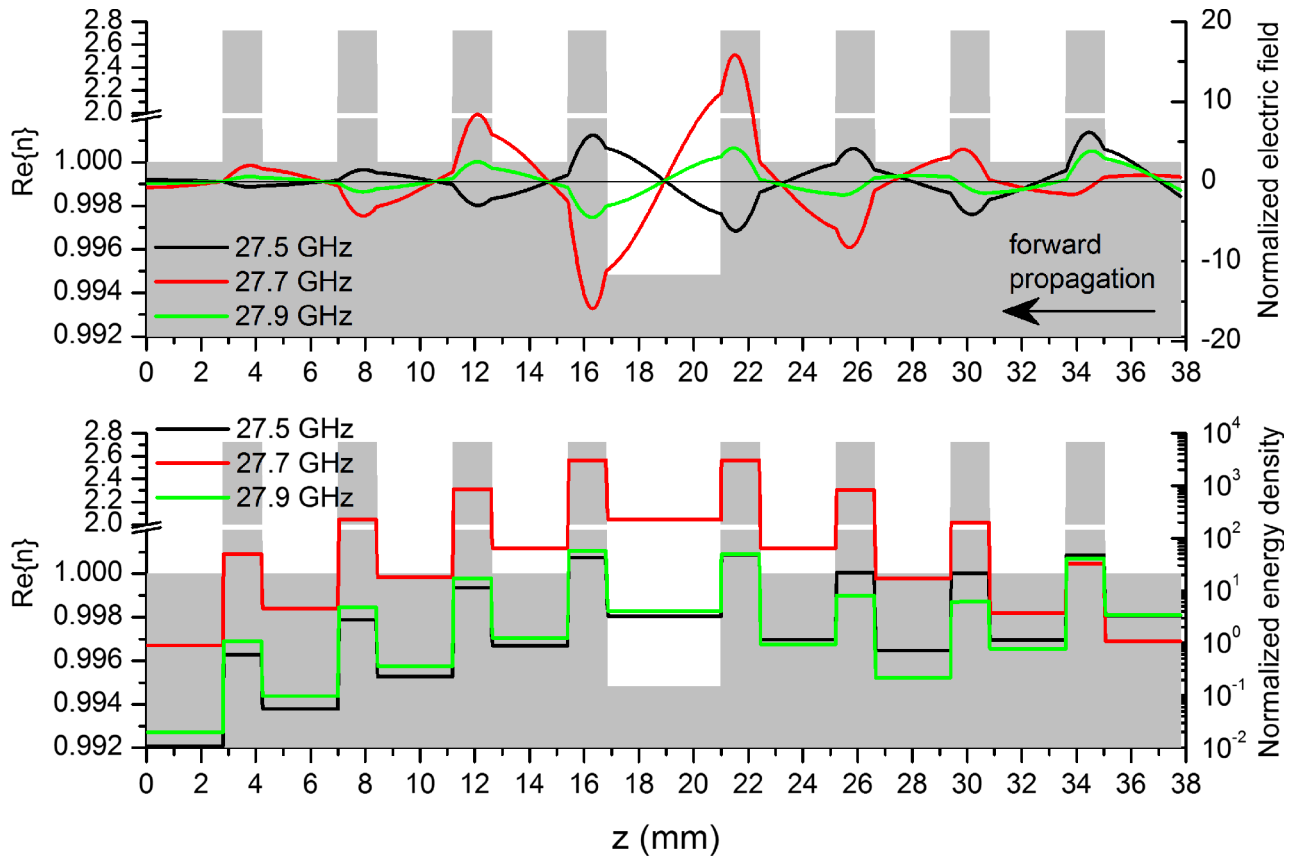


**Fig. 14.** Modeled electric field  $Re\{E\}$  (top) and energy density  $\varepsilon|E^2|/2$  (bottom) profiles as a function of position along the propagation axis, normalized to the corresponding values  $Re\{E\}$  and  $\varepsilon|E_+|^2/2$  of the forward-propagating wave at the point of entry into the crystal at  $z = 35$  mm. The profiles correspond to the case of uniform  $n_e = 1 \times 10^{11} \text{ cm}^{-3}$  shown in Figure 9, calculated at the defect peak frequency of 27.7 GHz as well as  $\pm 0.2$  GHz off this resonance. Also shown is the real component of the index of refraction (shaded). The crystal dimensions are the same as for Figure 8.

relative change appears to become greater as  $n_e$  decreases, but this is likely due to using a peak-finding algorithm that simply returns the frequency corresponding to the highest value for transmission. This value is sensitive to the discretization in frequency of the calculation. Other algorithms, such as a Lorentzian fit of the transmission spectrum, may be better suited to finding the peak when the shift is very small at low  $n_e$ .

## 5 Conclusions

The transmission spectrum of a one-dimensional photonic crystal with a plasma defect has been characterized experimentally over the microwave and near-terahertz range (26.5–600 GHz). The crystal consists of alternating layers of alumina and argon gas, with a built-in defect in the form of a void, i.e. one of the gas layers is thicker than the others. This defect creates several sharp transmission peaks within the stop bands of the spectrum. The center frequency of the first defect peak near 28 GHz shifts upwards when an AC plasma is generated inside the defect gas gap. For argon at 5 torr, the shift increases monotonically up to 20 MHz as the electron number density increases from zero up to  $3 \times 10^{10} \text{ cm}^{-3}$ . If the RMS current is kept

constant at a moderate value, then the shift increases with pressure from 5 to 20 torr. At high pressure and/or current, plasma heating is suspected to affect the peak shift via localization of the discharge, expansion of the defect gap, and expansion of the gas.

In addition to experiments, a numerical model of the crystal has been developed based on a transfer matrix method. Without plasma and for several crystal geometries, quantitative agreement between measured and modeled transmission spectra is found up to 250 GHz, and qualitative agreement is found at higher frequencies up to 600 GHz. With plasma filling the gas gap that includes the void defect, it is possible to establish a linear relationship between the defect peak shift and the electron number density. The model supports the idea that plasma heating diminishes the defect peak shift and shows that the shift is not sensitive to electron temperature nor to non-uniform  $n_e$  profiles.

The accuracy of this diagnostic technique, and in particular the lowest plasma density resolvable, will be limited by the lowest possible frequency shift measurable experimentally. In our facility, we found this to be about a few MHz, corresponding to an accuracy of measurement on the order of  $\Delta n_e = 10^9 \text{ cm}^{-3}$ . With better equipment,

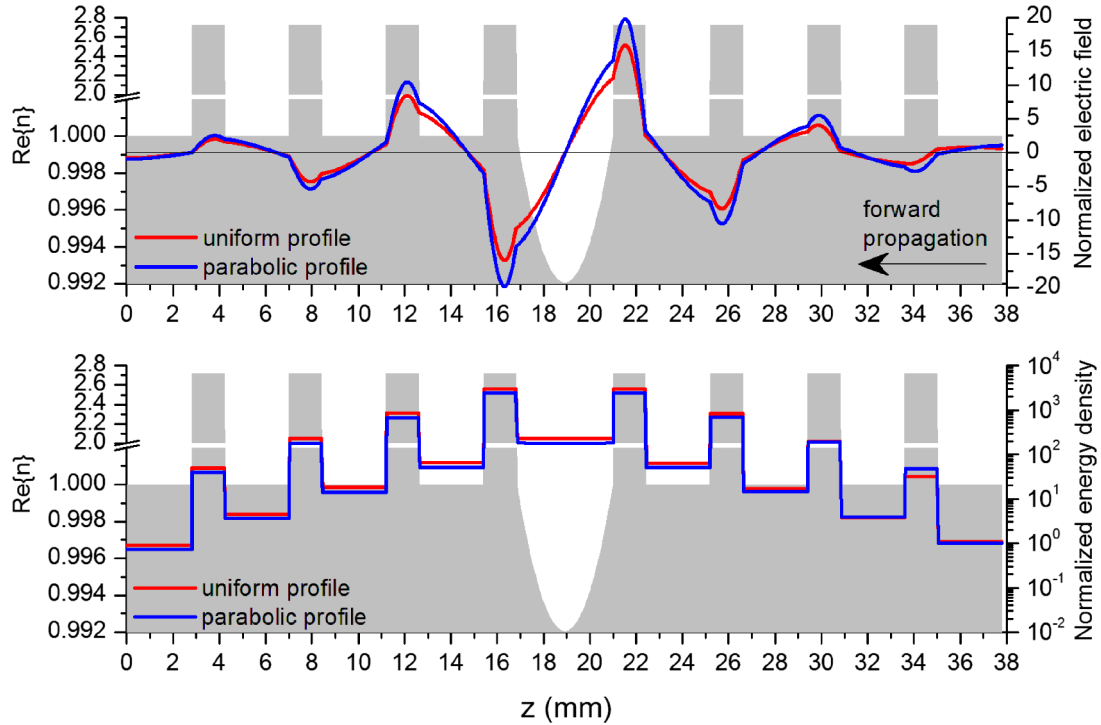


**Fig. 15.** Modeled electric field  $Re\{E\}$  (top) and energy density  $\varepsilon|E^2|/2$  (bottom) profiles as a function of position along the propagation axis, normalized to the corresponding values  $Re\{E\}$  and  $\varepsilon|E_+|^2/2$  of the forward-propagating wave at the point of entry into the crystal at  $z = 35$  mm. For the case of uniform  $n_e$ , the profiles are identical to those calculated in Figure 14 at the defect peak frequency of 27.7 GHz. For the case of non-uniform  $n_e$  according to equation (6), the profiles are calculated with  $n_{e,max} = 1.53125 \times 10^{11} \text{ cm}^{-3}$  and  $T_e = 30\,000$  K, also at 27.7 GHz. Also shown is the real component of the index of refraction for the variable  $n_e$  case (shaded). The crystal dimensions are the same as for Figure 8.

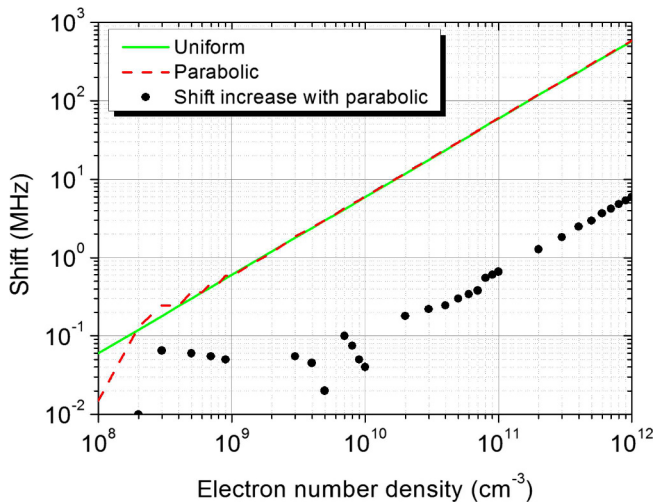


**Fig. 16.** Modeled shift of the defect peak frequency relative to the no-plasma frequency for a uniform  $n_e$  profile (solid line) and a parabolic  $n_e$  profile according to equation (6) for the same average  $n_e$  (dashed line), as a function of the electron number density for a plasma in Ar at 5 torr with  $T_e = 30\,000$  K. Also shown in is the increase in shift associated with the parabolic profile (symbols). The shift is determined by the frequency of maximum transmission of the peak profile (Python library Peakutils, “indexes” algorithm). The crystal dimensions are the same as for Figure 8.

and a more stable photonic crystal (control of temperature, etc.), a finer resolution may be possible and hence a greater sensitivity to even lower plasma densities may be possible.

This work has been supported by a Collaborative Research Project grant from the France-Stanford Center for Interdisciplinary Studies. Professor Cappelli acknowledges support through a Multidisciplinary University Research Initiative from the Air Force Office of Scientific Research.

### Author contribution statement

The contributions of each of the authors are as follows. D.Z.P. and M.A.C. conceived the project, led the experimental and modeling work, and wrote the manuscript. F.R. and D.Z.P. performed the terahertz transmission measurements. B.C.W., M.A.C., and D.Z.P. performed the microwave transmission experiments. D.R.B. and D.Z.P. adapted the model to the current work. D.Z.P. and M.A.C. analyzed the results.

### Appendix A

Here we summarize key details concerning the numerical model of the photonic crystal. As mentioned above, the

transfer matrix method used here follows that presented in [16]. The elementary transfer matrix from slab  $i$  to slab  $i+1$  is defined as:

$$\begin{bmatrix} E_{+,i} \\ E_{-,i} \end{bmatrix} = \mathbf{M}_i \mathbf{P}_i \begin{bmatrix} E_{+,i+1} \\ E_{-,i+1} \end{bmatrix}, \quad (\text{A.1})$$

where  $E_+$  and  $E_-$  are the amplitudes of the forward- and backward-propagating electromagnetic waves. We define the matching ( $\mathbf{M}_i$ ) and propagation ( $\mathbf{P}_i$ ) matrices as:

$$\mathbf{M}_i = \frac{1}{\tau_i} \begin{bmatrix} 1 & \rho_i \\ \rho_i & 1 \end{bmatrix}, \quad (\text{A.2})$$

$$\mathbf{P}_i = \begin{bmatrix} e^{jk_i l_i} & 0 \\ 0 & e^{-jk_i l_i} \end{bmatrix}. \quad (\text{A.3})$$

Here  $l_i$  is the thickness of slab  $i$ . The wavenumber is  $k_i = \omega n_i / c$ , where  $\omega$  is the angular frequency,  $c$  is the speed of light, and  $n_i$  is the index of refraction of slab  $i$ . The elementary transmission ( $\tau_i$ ) and reflection ( $\rho_i$ ) coefficients are:

$$\frac{1}{\tau_i} = \frac{1}{2} \left( 1 + \frac{k_i}{k_{i-1}} \right). \quad (\text{A.4})$$

$$\rho_i = \frac{1 - k_i / k_{i-1}}{1 + k_i / k_{i-1}}. \quad (\text{A.5})$$

The matrix in equation (A.1) is defined such that the upstream wave with index  $i$  is solved in terms of the downstream wave with index  $i+1$ . As such, solving for the entire crystal requires specifying conditions at the exit interface  $M+1$ , where no wave is reflected on the side that is outside the crystal:

$$\begin{bmatrix} E_{+,M+1} \\ E_{-,M+1} \end{bmatrix} = \frac{1}{\tau_{M+1}} \begin{bmatrix} 1 & \rho_{M+1} \\ \rho_{M+1} & 1 \end{bmatrix} \begin{bmatrix} E'_{+,M+1} \\ 0 \end{bmatrix}. \quad (\text{A.6})$$

Here,  $E'_{+,M+1}$  is the forward-propagating wave on the side of the  $M+1$  interface that is outside of the crystal. On the side that is inside the crystal,  $E_{+,M+1}$  and  $E_{-,M+1}$  are forward- and backward-propagating waves, respectively. The complete transfer matrix for the crystal ( $\mathbf{C}$ ) is thus:

$$\begin{aligned} \begin{bmatrix} E_{+,1} \\ E_{-,1} \end{bmatrix} &= \left( \prod_{i=1}^M \mathbf{M}_i \mathbf{P}_i \right) \mathbf{M}_{M+1} \begin{bmatrix} E'_{+,M+1} \\ 0 \end{bmatrix} \\ &\equiv \mathbf{C} \begin{bmatrix} E'_{+,M+1} \\ 0 \end{bmatrix}. \end{aligned} \quad (\text{A.7})$$

The fraction  $T$  of transmitted power at a given  $\omega$  is calculated using element  $c_{11}$  of  $\mathbf{C}$ :

$$T(\omega) = \frac{1}{|c_{11}|^2}. \quad (\text{A.8})$$

The transmission spectra shown in Sections 4.1 and 4.2 are constructed using equation (A.8) calculated over a frequency range.

## References

1. A.Y. Nikiforov, C. Leys, M. Gonzalez, J. Walsh, Plasma Sources Sci. Technol. **24**, 034001 (2015)
2. S. Hassaballa, K. Tomita, Y.K. Kim, K. Uchino, H. Hatanaka, Y.M. Kim, C.H. Park, K. Muraoka, Jpn. J. Appl. Phys. **44**, L442 (2005)
3. K. Urabe, H. Muneoka, S. Stauss, K. Terashima, Plasma Sources Sci. Technol. **23**, 064007 (2014)
4. X.P. Lu, M. Laroussi, Appl. Phys. Lett. **92**, 051501 (2008)
5. S. Muller, D. Luggenholtscher, U. Czarnetzki, J. Phys. D: Appl. Phys. **44**, 165202 (2011)
6. H.R. Griem, *Principles of Plasma Spectroscopy* (Cambridge, Cambridge University Press, 1997)
7. T. Orrière, E. Moreau, D.Z. Pai, J. Phys. D: Appl. Phys. **51**, 494002 (2018)
8. D.M. Packan, Repetitive nanosecond glow discharge in atmospheric pressure air, Ph.D. thesis, Stanford University, 2003
9. Y. Ito, O. Sakai, K. Tachibana, Plasma Sources Sci. Technol. **19**, 025006 (2010)
10. A. Shashurin, M. Shneider, A. Dogariu, R. Miles, M. Keidar, Appl. Phys. Lett. **96**, 171502 (2010)
11. B. Wang, M. Cappelli, Appl. Phys. Lett. **107**, 171107 (2015)
12. O. Sakai, T. Sakaguchi, T. Naito, D.-S. Lee, K. Tachibana, Plasma Phys. Control. Fusion **49**, B453 (2007)
13. J. Faith, S. Kuo, J. Huang, Phys. Rev. E **55**, 1843 (1997)
14. V. Arkhipenko, T. Callegari, L. Simonchik, J. Sokoloff, M. Usachonak, J. Appl. Phys. **116**, 123302 (2014)
15. V. Babitski, T. Callegari, L. Simonchik, J. Sokoloff, M. Usachonak, J. Appl. Phys. **122**, 083302 (2017)
16. S.J. Orfanidis, *Electromagnetic Waves and Antennas* (Rutgers University New Brunswick, NJ, 2002)
17. D.R. Biggs, M.A. Cappelli, Appl. Phys. Lett. **109**, 124103 (2016)
18. M.N. Afsar, K.J. Button, Proc. IEEE **73**, 131 (1985)
19. SIGLO database [www.lxcat.net](http://www.lxcat.net), Retrieved on January 19, 2018
20. G. Hagelaar, L. Pitchford, Plasma Sources Sci. Technol. **14**, 722 (2005)
21. Y.P. Raizer, *Gas Discharge Physics* (Berlin, Springer, 1991)
22. K. Takahashi, K. Miyamoto, J. Phys.: Conf. Ser. **441**, 012011 (2013)
23. J.D. Joannopoulos, S.G. Johnson, J.N. Winn, R.D. Meade, *Photonic Crystals: Molding the Flow of Light* (Princeton university press, 2011)